Journal of The
Electrochemical Society

Impact of the Plasticizer Content on the Lithium Plating Behavior in Lithium Polymer Batteries

To cite this article: Katrin Geng *et al* 2026 *J. Electrochem. Soc.* **173** 150505

Journal of The Electrochemical Society, 2026 **173** 150505

Impact of the Plasticizer Content on the Lithium Plating Behavior in Lithium Polymer Batteries

Katrin Geng,[1,2,=] Vivaan Patel,[3,4,=] Dominik Steinle,[1,2,=] Pallab Barai,[5] Medina Jasarevic,[1,2] Michael Bowen,[3,4] Venkat Srinivasan,[6,*,z] Nitash Balsara,[3,4,*] and Dominic Bresser[1,2,7,*]

[1]*Helmholtz Institute Ulm (HIU), 89081 Ulm, Germany*
[2]*Karlsruhe Institute of Technology (KIT), 76131 Karlsruhe, Germany*
[3]*Department of Chemical and Biomolecular Engineering, University of California, Berkeley (UCB), CA 94720, United States of America*
[4]*Materials Sciences Division, Lawrence Berkeley National Laboratory (LBNL), Berkeley, CA 94720, United States of America*
[5]*Applied Materials Division, Argonne National Laboratory (ANL), Lemont, IL 60439, United States of America*
[6]*Chemical Sciences and Engineering Division, Argonne National Laboratory (ANL), Lemont, IL 60439, United States of America*
[7]*Ulm University (UUlm), 89069 Ulm, Germany*

At present, the only commercial lithium-metal battery (LMB) technology is based on polyethylene oxide (PEO) based electrolytes. However, its limited ionic conductivity at ambient temperatures requires the operation (discharge and charge) at elevated temperatures of around 60 °C–80 °C, i.e., close to and above the melting point of PEO. Herein, we investigate the impact of incorporating varying amounts of tetraethylene glycol dimethyl ether serving as chemically identical plasticizer to enhance the ionic conductivity also at lower temperatures. A comprehensive comparison of the physicochemical, electrochemical, and mechanical properties is conducted via complementary experimental and theoretical studies, with a particular focus on the impact on the morphology of the deposited lithium using ex situ X-ray tomography. The results reveal that the mechanical properties play a key role for achieving a homogeneous and smooth lithium deposition. These insights are anticipated to contribute to further optimized polymer-based electrolytes for next-generation LMBs.

[DOI: 10.1149/1945-7111/ae8ebe]

Manuscript submitted February 12, 2026; revised manuscript received July 15, 2026. Published August 3, 2026.

Supplementary material for this article is available online

High-energy density batteries—in particular lithium-ion batteries (LIBs)—are ubiquitous in our modern life, facilitating energy storage in mobile devices like mobile phones and electric vehicles.[1] Lithium metal batteries (LMBs) promise to be the next generation of high-energy-density batteries, offering theoretical energy densities several times higher—and practical energy densities 70%–80% greater—than those of current LIBs.[2–4] However, during charging, nonuniform lithium metal plating often leads to the formation of dendritic structures, posing a significant safety risk.[5]

One promising strategy to improve the safety of LMBs is to replace the conventional flammable organic liquid electrolyte with solid polymer electrolytes.[6] Among these, polyethylene oxide (PEO) is the most extensively studied, largely due to its good interfacial contact and high electrochemical stability.[7] However, PEO exhibits much lower ionic conductivity at room temperature compared to liquid electrolytes. For example, the ionic conductivity of PEO with lithium bis(trifluoromethane sulfonyl)imide (LiTFSI) at an ethylene oxide-to-lithium salt molar ratio of 10:1 is approximately 0.02 mS cm^{-1} at 20 °C,[8] whereas for a typical liquid electrolyte containing EC:EMC (3:7 wt/wt) with 1 mol kg^{-1} $LiPF_6$, it is as high as 8 mS cm^{-1}.[9]

One strategy to approach this limitation is the incorporation of a liquid plasticizer into crosslinked polymer networks, also commonly referred to as gel polymer electrolytes.[10] The idea behind this approach is to unite the advantages of liquid and solid electrolytes, i.e., high ionic conductivity and high mechanical stability, respectively.[11] A suitable plasticizing agent for crosslinked PEO is tetraethylene glycol dimethyl ether (or tetraglyme, TEGDME) because it exhibits a comparable electrochemical stability window and a high thermal stability up to 200 °C.[12,13] According to the literature, plasticizing PEO with TEGDME remarkably alters its physicochemical properties. For example, according to Yang et al.[7] and Lehmann et al.,[13] plasticizing PEO with TEGDME promotes the segmental motion of the PEO chains and reduces the glass transition temperature, thus facilitating ion transport. Moreover, the solvation of lithium ions by TEGDME reduces the interaction between the lithium salt and the polymer chains, and offers a fast, alternative ion transport pathway through TEGDME.[7,13]

This positive impact on ionic mobility upon liquid addition, however, is typically accompanied by a significant reduction in mechanical stiffness.[14] Although crosslinking can increase the dimensional stability and mechanical modulus of plasticized polymer electrolytes, higher mechanical stiffness often comes at the cost of reduced ionic conductivity.[10,13] This trade-off is particularly relevant in the context of dendrite suppression. Some studies on lithium dendrite growth suggest that improved ionic conductivity and diffusivity—achievable through plasticization—can promote more uniform lithium deposition and reduce dendrite formation by homogenizing the lithium-ion flux, thereby minimizing local current density hotspots.[15–17] Conversely, according to the theoretical work by Monroe and Newman[18] based on linear elasticity theory, suppressing dendritic lithium growth requires solid electrolytes with high shear modulus values—in the megapascal range for materials with a Poisson's ratio similar to PEO. While this theory has reached its limits for inorganic solid electrolytes like LLZO, where, despite the high modulus of the bulk material, dendrites grow along grain boundaries,[19,20] its validity for polymer-based electrolytes remains ambiguous. For instance, Khurana et al.[17] have presented a crosslinked polymer electrolyte with a modulus of only $G' \approx 10^5$ Pa and remarkable dendrite growth resistance, suggesting that a high modulus polymer

[=] These authors contributed equally to this work.
[*] Electrochemical Society Member.
[z] E-mail: dominic.bresser@kit.edu; nbalsara@berkeley.edu; vsrinivasan@anl.gov

electrolyte is not a strict requirement for the control of dendrite proliferation. However, Röring et al.[21] reported that the mechanical properties play an essential role for the homogeneity of the lithium deposition and the suppression of dendritic lithium growth. Consequently, the net effect of, e.g., adding a plasticizer on a potential lithium dendrite growth remains an open question. In fact, also the solid electrolyte interphase (SEI) may influence lithium nucleation and growth through its ionic transport properties, mechanical integrity, chemical composition, and spatial homogeneity.[22,23]

In this study, we elucidate how the plasticizer content in crosslinked PEO-based polymer electrolytes and the resulting changes of the mechanical properties affect the lithium plating morphology and dendrite formation. To this end, we perform a comprehensive electrochemical and mechanical characterization of three polymer-based electrolytes with varying TEGDME content. Lithium plating behavior is analyzed by electrochemical impedance spectroscopy (EIS), tomography, and computational modeling. This combined approach enables the identification of the dominant factors influencing the morphology of plated lithium in plasticized polymer electrolytes.

Methods

Polymer electrolyte fabrication.—Polymer membranes were prepared via a solvent-free method previously reported in the literature (e.g., Refs.24, 25) Polymer electrolytes consisting of polyethylene oxide (PEO, M_w = 4000 000 g mol^{-1}), tetraethylene glycol dimethyl ether (TEGDME), lithium bis(trifluoromethane sulfonyl)imide (LiTFSI), and benzophenone were prepared at HIU in three different PEO:TEGDME ratios, being 90:10 wt.%, 70:30 wt.%, and 50:50 wt.%. LiTFSI, the conducting salt, and benzophenone, serving as crosslinking initiator, were added to yield an ethylene oxide-LiTFSI-benzophenone molar ratio of 100:10:1. Before mixing, all solid materials were dried under vacuum at 10^{-3} bar: PEO at 50 °C for 48 h, LiTFSI at 120 °C for 24 h, and benzophenone at room temperature for 24 h. The dried materials were only handled in a dry room (dew point ≈−70 °C ≡ <2 ppm H_2O). The materials were mixed until a cohesive, rubbery mass was obtained, vacuum-sealed in a pouch bag, and annealed at 90 °C (in a Binder E 28 oven) overnight. The next day, the materials were hot-pressed (Polystat 200 T, Servitec) at 100 °C in a multistep process starting at ca. 7 bar for one minute, followed by 3 min at 10 bar in the 50:50 case, 14 bar in the 70:30 case, and 18 bar in the 90:10 case, yielding membranes with a thickness of ca. 100 μm. Subsequently, the membranes were exposed to UV light (UVACUBE 100, hönle uv technology) from both sides for 4 min each to initiate cross-linking. These membranes were also shipped to UCB.

Mechanical testing.—For the mechanical analysis of the polymer membranes, tensile strength measurements were performed at the material testing machine ZwickiLine (ZwickRoell) according to the ISO 527 series of standards to determine the elastic moduli. Standardized polymer pieces (dog bone shape type 1B with a gauge length of 50 mm) were punched out in a dry room (dew point ≈−70 °C ≡ <2 ppm H_2O), using a bent lever-cutting press (ZCP020, ZwickRoell). The tensile strength measurements were performed at room temperature under an inert atmosphere (in a glove bag flushed several times with argon). The polymer films were stretched at 5 mm min^{-1} until a pre-load of 0.1 MPa was reached, held for ten seconds, and then stretched continuously. Between 0.25% and 25% strain, the polymer membranes were elongated at 1 mm min^{-1} and afterwards at 200 mm^{-1} until either the material tore or the soft end of the machine was reached. The elastic or Young's modulus was determined between 0.25% and 20% strain and was averaged over at least three measurements for each material.

Cell fabrication.—At HIU, pouch cells were built under dry room conditions (dew point ≈−70 °C ≡ <2 ppm H_2O). Cells were typically assembled in a Li||Li geometry with an active cell area of 1.131 cm^2, as described in the following. A polymer electrolyte piece (thickness: ∼100–120 μm; diameter: 16 mm) was placed between a lithium stripe (Honjo Metal Co., thickness: 300 μm; width: 20 mm) and a punched lithium disk (diameter: 12 mm). The lithium stripe and disk were attached to the nickel current collector stripes within the pouch cell housing. For the conductivity measurements, a blocking stainless steel||stainless steel pouch cell with an active area of 4 cm^2 was used instead. For this, a square-shaped polymer electrolyte piece was placed between two stainless steel stripes with a width of 20 mm each. After cell assembly, the pouch cells were sealed under vacuum (Audionvac VMS 163).

At UCB, Li||Li pouch cells were assembled in an argon-filled glovebox. For measuring electrochemical properties (i.e., conductivity, diffusion coefficient, transference number), two 6.35 mm lithium electrodes were punched out from a lithium metal foil (MSE supplies). An electrolyte disc (diameter: 8 mm) was punched out from the given electrolyte samples, prepared at HIU. The electrolyte was layered between the lithium electrodes and mechanically pressed to ensure good contact. The entire assembly was placed between nickel tabs and sealed in pouch foil under vacuum. For the unidirectional plating and tomography experiments, the diameter of the lithium electrodes and electrolyte was 9.5 mm and 10.1 mm, respectively. The assembly was placed between two stainless steel shims for mechanical support and attached with aluminum tabs. The cell was sealed in pouch foil under vacuum.

Electrochemical testing.—All electrochemical measurements were conducted with a VMP-3e potentiostat system from Biologic. The experiments were repeated three times and the results averaged.

Transference number.—Before any electrochemical properties were measured, the cells were rested for at least 100 h (100 h at UCB and 250 h at HIU) at open circuit potential at 40 °C. Transference number measurements were carried out via the Bruce–Vincent method in non-blocking Li||Li cells.[26–28] In brief, a constant potential of 10 mV was applied for ⩾5 h until a steady-state current, i_{ss}, was achieved. EIS was used to measure the bulk and interfacial impedance (R_b and R_i) before and after polarization. The initial current, i_Ω, is calculated using Ohm's Law in Eq. 1:

$$i_\Omega = \frac{\Delta V}{R_{i,0} + R_{b,0}} \quad [1]$$

$R_{b,0}$ and $R_{i,0}$ represent the initial bulk and interfacial resistances, respectively. The steady-state transference number, t_+, was calculated using the following Eq. 2:

$$t_+ = \frac{i_{ss}\left(\Delta V - i_\Omega R_{i,0}\right)}{i_\Omega\left(\Delta V - i_{ss} R_{i,ss}\right)}. \quad [2]$$

Diffusion coefficient.—Restricted diffusion coefficient measurements were obtained by using the concentration polarization curves from the transference number experiments. The cells were relaxed for 12 h after the 10 mV polarization. This relaxation potential decay was fitted to Eq. 3:

$$U\left(t\right) = k_0 + ae^{-bt} \quad [3]$$

where k_0, a, and b are fitted parameters. The salt diffusion coefficient can then be found using Eq. 4. L represents the electrolyte thickness.

$$D = \frac{L^2 b}{\pi^2}\ . \quad [4]$$

Fitting was conducted by incrementally increasing the lower bounds of time until the nondimensional number α (Eq. 5) reached a value greater than 0.05.[29]

$$\alpha = \frac{Dt}{L^2}. \quad [5]$$

Ionic conductivity.—To measure the ionic conductivity, blocking stainless steel||stainless steel pouch cells were used. These cells were equilibrated in a Binder climatic chamber for at least 2 h prior to the EIS measurements, which were conducted using a Solartron SI 1260 impedance analyzer. EIS measurements were performed starting at 90 °C, decreasing in 10 K increments down to 10 °C, followed by a return to 90 °C in the same stepwise manner. This temperature cycling was carried out to identify and rule out potential hysteresis-related anomalies. The frequency range for the EIS measurements spanned from 1 MHz to 100 Hz. Conductivity values reported for UCB were determined using the bulk resistance obtained from transference number measurements. The impedance spectra were fitted using a classical equivalent circuit model for symmetrical blocking cells, consisting of a constant phase element (CPE) in series with a resistor (R), to extract the resistance values. The ionic conductivity σ was then calculated using Eq. 6:

$$\sigma = \frac{L}{RA}. \quad [6]$$

Limiting current density.—For determining the limiting current of the polymer electrolyte samples, symmetric Li||Li pouch cells were assembled and tested using linear sweep voltammetry using an SI 1287 impedance analyzer from Solartron. The cells were tested at 40 °C in a climatic chamber. Before the sweep voltammetry test, the cells were stored at 40 °C for 12 h to ensure thermal equilibration of the cells. The sweep rate was set to 0.1 mV s^{-1}. The limiting current was approximated by the appearance of a plateau-like behavior of the data curve resulting from plotting the current density versus the swept potential.

Unidirectional plating experiment with EIS.—For the unidirectional plating experiment at 40 °C, a current density of 50 μA cm^{-2} was applied for 250 h and the overpotential was recorded. Every 5 h, after 5 min rest, EIS was performed in the frequency range from 1 MHz to 1 Hz with an excitation amplitude of 10 mV. At UCB, the unidirectional plating experiment was conducted using the tomography cell setup. The cell was then imaged using hard X-ray microtomography without disassembling. The same experiment was conducted at HIU under open circuit conditions (during storage) for 250 h.

The obtained EIS spectra were fitted between 0.2 MHz and 20 Hz with the software RelaxIS3 (rhd instruments) using the following equivalent circuit model R-(R)(CPE)-(R)(CPE) with the three R values being a resistor corresponding to the bulk resistance, the charge transfer resistance, and the SEI resistance, respectively, and CPE representing a constant phase element. The distribution of relaxation times analysis (DRT) was also performed using RelaxIS3 with the regularization parameter λ carefully chosen at 0.001 following the description in Ref.30

X-ray tomography.—The cells were imaged at the Advanced Light Source (ALS) beamline 8.3.2 using hard X-ray microtomography. Monochromatic X-rays with an energy of 22 keV were transmitted through the sample and converted to visible light using a scintillator. The image was magnified using a 4× lens and converted to a digital image using an optical microscope. The pixel size is approximately 1.62 μm for a 4× lens. The sample was incrementally rotated 180° to collect a total of 1313 projections. Cross-sectional slices were reconstructed and then rendered using ImageJ. A subsection of the imaged cell with an area of 0.54 cm^2 (0.74 × 0.74 cm) was used to manually classify and count each dendritic feature.

Subsections measuring approximately 750 μm in all three spatial dimensions were randomly selected from each of the three samples. Each voxel was then assigned a lithium or polymer tag using the Weka 3D Segmentation plug-in for ImageJ. Remaining dendrites, holes, and other spatial outliers not indicative of the global behavior of each interface were removed manually in Avizo. 3D renderings of each sample were generated in Avizo as well.

Modeling.—In order to capture the dynamic growth of dendritic protrusions, charge, mass, and momentum balance relations are solved within a computational domain with moving boundary capabilities. The computational domain includes the polymer electrolyte, the deposited lithium layer, and a small portion of the lithium-metal electrode, which is demonstrated in Fig. S6a. The electrolyte is denoted by blue, the lithium deposit layer is shown in magenta, and the lithium-metal electrode is demonstrated by the red region.

During the plating of lithium, current and lithium-ion flow occurs from the top of the electrolyte, while lithium is deposited at the bottom after the electrochemical reduction process:

$$Li^+ + e^- \rightarrow Li. \quad [7]$$

Transport of lithium ions within the polymer electrolyte occurs through both migration and diffusion, which is captured using the concentration solution theory. Nonuniform deposition of lithium at the bottom electrode leads to nonuniform displacement of the electrode|electrolyte interface, which effectively leads to compressive stress generation within both the electrode and the electrolyte domains. Momentum balance relations capable of capturing large deformations are solved to estimate the deformation and stress evolution within the electrode and electrolyte regions under mechanical equilibrium. The impact of mechanical stress on the electrochemical deposition of lithium is modeled through a modified Butler–Volmer expression (i_{BV}, Eq. 8, compare Refs.18,31,32)

$$i_{BV} = Fk_{ref}c_e^{0.5}\exp\left(\Delta\mu_{e^-}/2RT\right)\cdot\left[\exp\left(F\eta_s/2RT\right) - \exp\left(-F\eta_s/2RT\right)\right]. \quad [8]$$

Here, F is the Faraday constant, k_{ref} indicates the reaction rate constant, c_e denotes the electrolyte salt concentration, R indicates the universal gas constant, T is temperature, $\Delta\mu_{e^-}$ is the stress-induced electrochemical potential term, and η_s is the surface overpotential. The surface overpotential is defined as, $\eta_s = \phi_s - \phi_e - U_{Li} + \left(\Delta\mu_{e^-}/F\right)$, where ϕ_s is the potential in lithium electrode or deposit layer adjacent to the electrolyte, ϕ_e is the potential in the electrolyte adjacent to the electrode, and U_{Li} indicates the open circuit potential for lithium deposition (in general, $U_{Li} \sim 0.0$ V). The stress induced electrochemical potential is defined according to Refs.32,33 as:

$$\Delta\mu_{e^-} = \bar{V}_{Li}p_{Li} - \bar{V}_{Li^+}p_{Li^+} \quad [9]$$

where, $\bar{V}_{Li}$ is the partial molar volume of lithium metal, $\bar{V}_{Li^+}$ is the partial molar volume of lithium ions within the electrolyte, p_{Li} and p_{Li^+} are the pressure in the metal electrode and solid electrolyte due to nonuniform deposition. Stress evolution within the lithium metal electrode is assumed to follow elastic–plastic constitutive relations. The deposit layer is assumed to be mechanically stiff, and the stresses within the top of the lithium electrode is considered as the stress within the lithium adjacent to the electrolyte. The detailed governing equations, corresponding boundary conditions, constitutive relations, and the list of parameters used in the model are provided within the Tables S3 and S4.

In order to estimate the lithium deposition induced vertical deformation $\left(d_{Li}\right)$ of the electrode|electrolyte interface, only the excess current at and around the peak of the protrusion is taken into consideration:

$$d_{Li} = \max\left(0.0, \left(\text{abs}\left(i_{BV}\left(x\right)\right) - \text{abs}\left(i_{BV}\left(L\right)\right)\right)\right)\cdot\left(\bar{V}_{Li}/F\right) \quad [10]$$

where, $i_{BV}\left(x\right)$ is the Butler–Volmer reaction current along the x-direction, and $i_{BV}\left(L\right)$ is the reaction current density at the very end of

the domain $(x = L)$. Since reduction of the lithium ions occur at the electrode, the sign of the Butler–Volmer reaction current is negative. The "abs" function helps to convert the negative reaction current to positive value. No backward movement of the electrolyte layer is modeled here. The reaction current density at $x = L$ is considered to be close to the applied current. In order to satisfy balance of the electrolyte salt before and after the deformation of the electrolyte domain, an extra mass balance step is implemented:

$$V^{n+1} \cdot c_e^{n+1} = V^n \cdot c_e^n \quad [11]$$

where, n indicates the timestep, V is the volume of the electrolyte domain, and c_e denotes the salt concentration in the electrolyte domain. This is implemented as a separate solve conducted after each of the lithium deposition induced mechanical deformation of the electrode and electrolyte domains.

Even though an updated Lagrangian (UL) framework is implemented for capturing the geometric nonlinearity associated with the large deformation of the electrode and electrolyte domains, the elastic–plastic material nonlinearity of the lithium-metal electrode is captured using a linear framework. The nonlinear strain-displacement relations are given as:

$$\varepsilon_{ij}^{tot} = \frac{1}{2}\left(\frac{\partial u_i}{\partial x_j} + \frac{\partial u_j}{\partial x_i} + \frac{\partial u_k}{\partial x_i}\frac{\partial u_k}{\partial x_j}\right) \quad [12]$$

where, ε_{ij}^{tot} indicates the total strain, u_i is the displacement along the ith direction, and x_i is the coordinate for the ith direction. The PEO-TEGDME solid electrolyte is assumed to deform only elastically, where the elastic $\left(\varepsilon_{ij}^{el}\right)$ and plastic $\left(\varepsilon_{ij}^{pl}\right)$ strains of the metal electrode is considered additive.

$$\varepsilon_{ij}^{tot} = \varepsilon_{ij}^{el} + \varepsilon_{ij}^{pl}. \quad [13]$$

Plastic deformation of the lithium-metal electrode starts once the stress exceeds the yield strength, and the magnitude of yield strength is adopted from the existing literature measured on bulk materials under tensile as well as compressive conditions.

Results and Discussion

Electrochemical and mechanical characterization.—Three crosslinked plasticized polymer electrolyte samples with different PEO:TEGDME weight ratios—90:10, 70:30, and 50:50—all containing LiTFSI as conducting salt, were investigated in this study. This work consists of several cross-validated experiments conducted at the Helmholtz Institute Ulm (HIU) and University of California Berkeley (UCB). Figure 1a shows the ionic conductivity (σ) measured over a temperature range from 10 °C to 90 °C in 10 °C increments at HIU.

For all three materials, the conductivity increases with an increasing temperature. The 90:10 sample exhibits the most pronounced increase from 10 °C to 40 °C, which corresponds to crystalline phases becoming amorphous.[34] This sharp increase in conductivity at lower temperatures observed in the 90:10 sample is not present in the 70:30 and 50:50 materials, which contain higher amounts of TEGDME. This is likely due to the ability of TEGDME to infiltrate the PEO matrix, facilitate the separation of PEO chains, alter the solvation environment of the salt ions, and modify the overall matrix structure, thereby reducing crystallinity.[13] When comparing the ionic conductivity values between the different electrolyte compositions (90:10 in blue, 70:30 in purple, and 50:50 in red), it is apparent that an increased TEGDME content results in higher conductivities across the whole temperature range. To verify this result, the ionic conductivity was also determined independently at UCB at 40 °C, which largely confirmed the conductivity values from HIU (compare Fig. 1a). Increasing the TEGDME content from 10 wt.% to 50 wt.% (relative to PEO) effectively increases the conductivity by approximately a factor of five. Hence, the results from both laboratories confirm a consistent trend of rising σ with an increasing TEGDME content. (UCB measured $\sigma(90{:}10) = 0.13 < \sigma(70{:}30) = 0.30 < \sigma(50{:}50) = 0.79$; HIU measured $\sigma(90{:}10) = 0.17 < \sigma(70{:}30) = 0.44 < \sigma(50{:}50) = 0.80$ mS cm^{-1}). This trend of increasing plasticizer amount contributing to an increased σ is well established in the literature.[13,35] The ionic conductivity values also align with those reported in the literature for systems with similar composition.[35–37]

Figure 1b shows the diffusion coefficient D independently determined at UCB and HIU. According to the literature, a larger TEGDME content is expected to enhance not only the ionic conductivity, but also the diffusion owing to an increased ion mobility.[36] Restricted diffusion measurements are, however, sensitive to several experimental factors. For example, small inaccuracies in electrolyte layer thickness directly affect the calculated values, while differences in data acquisition rates can alter the fitting quality. In addition, variations in cell setup between laboratories may introduce further deviations. Since the experimental conditions at UCB and HIU were not identical, discrepancies between the two datasets are not unexpected. Nevertheless, both datasets clearly confirm the trend of faster diffusion with more liquid plasticizer: $D(90{:}10) < D(70{:}30) < D(50{:}50)$. The measured diffusion coefficients range from approximately 1.0 10^{-8}–1.5 10^{-7} cm^2 s^{-1}. Porcarelli et al.[37] measured a diffusion coefficient of 2.1 10^{-8} cm^2 s^{-1} for PEO:TEGDME 50:50 at 25 °C, which aligns well with our results at 40 °C that are somewhat larger due to the known increase in D with temperature.[36] Wang et al.[36] reported a diffusion coefficient of 3.4 10^{-7} cm^2 s^{-1} for a 70:30 composition at 60 °C, which is in a similar range to what was measured at UCB at 40 °C. Altogether, the comparison with previously reported studies confirms that the diffusion coefficient values we found fall within the expected range.

The Bruce–Vincent lithium-ion transference number, t_+, was determined using the approach described in Refs.26–28 (Fig. 1c, Table S1). While the ionic conductivity and diffusion coefficient increase with higher TEGDME content (Figs. 1a and 1b), the lithium-ion transference number (Fig. 1c), does not exhibit a clear trend. In all three compositions, t_+ lies in the range from 0.05 to 0.15, which is in good agreement with previous studies,[38] indicating that in general the anion mobility largely contributes to the overall ionic conductivity. This behavior is not ideal, though, because it exacerbates concentration gradient formation in the presence of an electric field, which can promote dendritic lithium plating.

To complete the characterization of the ionic transport properties of these plasticized polymer electrolytes, we also determined the limiting current density (i_L). Figure 1d shows the results from linear sweep voltammetry experiments conducted at HIU. As the potential was steadily increased, the current rose sharply, transitioning into a current plateau at around 0.3 V vs Li$^+$ /Li. These plateaus correspond to limiting current densities (i_L) of 0.41 mA cm^{-2}, 0.87 mA cm^{-2}, and 1.7 mA cm^{-2}, for the 90:10, 70:30, and 50:50 materials, respectively. Normalizing by thickness, d, allows for better comparison across many electrolytes. The corresponding length-normalized limiting currents are $i_L d(90{:}10) = 0.005$ mA cm^{-1}, $i_L d(70{:}30) = 0.010$ mA cm^{-1}, and $i_L d(50{:}50) = 0.020$ mA cm^{-1}. The observed increase in limiting current density with more plasticizer content in the order $i_L(90{:}10) < i_L(70{:}30) < i_L(50{:}50)$ can be attributed to an enhanced ion mobility and ionic conductivity, enabling the electrolyte to supply ions to the reaction interface and to sustain higher current densities without inducing cell failure.[14] In a recent study investigating a PEO:TEGDME material in a 50:50 ratio, also with LiTFSI as conducting salt, Bertoli et al.[39] found a limiting current density of 1.45 mA cm^{-2}, which closely matches our results. Additionally, the length-normalized limiting current density, $i_L d$, can

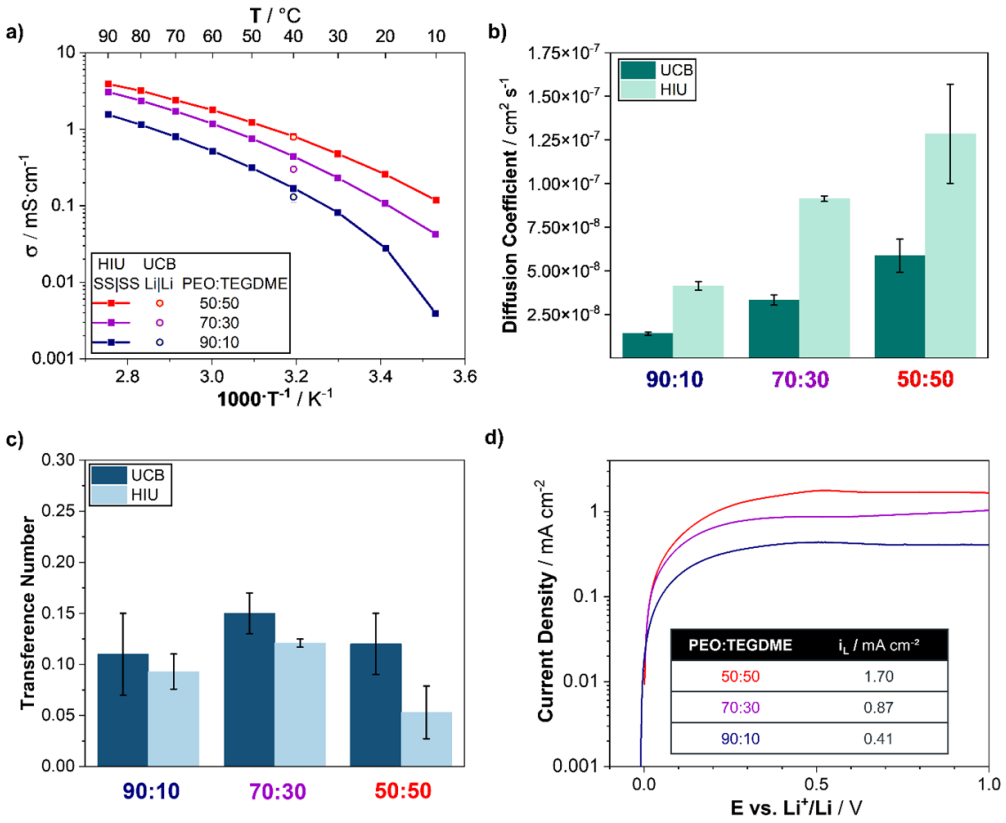

Figure 1. Electrochemical characterization of three plasticized polymer electrolytes with LiTFSI in PEO:TEGDME weight ratios of 90:10 (blue), 70:30 (purple), and 50:50 (red) analyzed at UCB and at HIU. (a) Ionic conductivity measurements conducted from 10 °C to 90 °C at HIU, independently validated at 40 °C at UCB. (b) Diffusion coefficient measurements for all three compositions at 40 °C, obtained in both laboratories. (c) Transference number results for all three compositions acquired in both laboratories in non-blocking cell setups. (d) Linear sweep voltammetry (LSV) from 0 to 1.0 V vs Li^+/Li conducted at HIU to determine the limiting current density for all three compositions at 40 °C.

also be approximated by the dilute solution theory using Eq. 14:

$$i_{\text{lim}}d = \frac{2cDF}{(1 - t_+)} \quad [14]$$

where c is the salt concentration, D is the diffusion coefficient, F is Faraday's constant, and t_+ is the transference number. The average salt concentration was determined to be 1.73 mol l^{-1}. Using the average diffusion coefficients and transference numbers for each electrolyte, $i_L d$ for the 90:10, 70:30, and 50:50 electrolytes were 0.0052 mA cm^{-1}, 0.013 mA cm^{-1}, and 0.022 mA cm^{-1}, respectively. These are in very good agreement with the experimental values reported above.

To complement the electrochemical analysis, the electrolyte materials were characterized mechanically by performing tensile strength tests. Figures 2 and S1 show the stress–strain curves for the three electrolytes with varying TEGDME content.

By linear fitting between 0% and 20% strain, the elastic moduli were determined to be 0.62 ± 0.05, 0.31 ± 0.05, and 0.13 ± 0.03 MPa for the 90:10, 70:30, and 50:50 compositions, respectively. As evident from Fig. S1, also the ultimate tensile strength is reduced with higher TEGDME content. These results clearly demonstrate that increasing the fraction of TEGDME significantly reduces the mechanical stiffness and strength of the polymer electrolyte. In the literature, dry PEO-LiTFSI-based electrolytes, especially when crosslinked, reach higher moduli with the shear modulus being in the range of 1–10 MPa, which translates into a Young's modulus in the range of 3–30 MPa (assuming a Poisson's ratio of 0.5).[40] For PEO-LiTFSI polymer electrolytes plasticized or modified with additives (e.g., succinonitrile[41] or polyhedral oligomeric silsesquioxane-polyethylene glycol[42]), Young's modulus values in the range of 0.19–1 MPa were reported, agreeing well with the range measured herein.[41,42]

Overall, the electrochemical characterization has shown that increasing the TEGDME content generally favors the ion transport properties, resulting in higher limiting current densities. However, there is a concomitant reduction of the mechanical stability, as evidenced by the decreased Young's moduli. These findings raise important questions about how the trade-off between enhanced ion transport and reduced mechanical modulus may influence lithium deposition during battery operation. To explore this, the following section discusses the expected implications of these properties on the potential growth of dendritic lithium deposits.

In theory, high ionic conductivities and diffusion coefficients are beneficial for inhibiting lithium dendrite formation. Fast diffusion enables a more uniform lithium-ion distribution, therefore facilitating a homogeneous ion supply for homogeneous lithium plating. Fast ionic conductivity reduces any potential concentration polarization, delaying the onset of ion-depletion near the electrode surface—a key factor in dendrite formation—as also shown by the increase in limiting current density.[43,44] Following these implications from the electrochemical characterization, one would expect reduced dendrite growth with larger plasticizer portions. On the other hand, as mentioned above, an earlier study by Monroe and Newman[18] suggests that a higher Young's modulus can be an effective way for inhibiting dendrite growth due to the physical sturdiness of the solid electrolyte. Considering that the mechanical

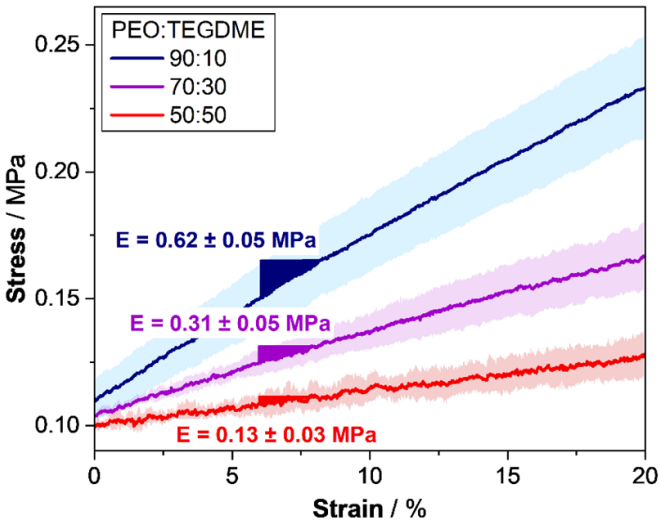

Figure 2. Mechanical characterization of the three plasticized polymer electrolytes with LiTFSI in PEO:TEGDME weight ratios of 90:10 (blue), 70:30 (purple), and 50:50 (red). Tensile tests were performed thrice per material at room temperature. The resulting stress–strain curves were averaged and linearly fitted between 0% and 20% strain to determine the Young's moduli, as indicated in the figure.

stiffness decreased with more TEGDME, one would expect a higher propensity for dendrite growth with larger plasticizer content. While the electrochemical characterization suggests a more homogenous lithium deposition for an increasing TEDGME content, the mechanical characterization suggests the opposite trend.[45,46] Therefore, it is necessary to conduct long-term plating experiments to analyze the overall impact of the TEGDME content on the lithium plating behavior.

Unidirectional lithium plating experiment.—To experimentally assess how the plasticizer content in the PEO-based electrolytes impacts the lithium plating behavior, lithium was plated unidirectionally in symmetric Li||Li cells containing the three different PEO:TEGDME compositio

ns, i.e., 90:10, 70:30, and 50:50. During this experiment, the plating behavior was investigated by EIS and overpotential measurements. Figures 3a–3c (measured at UCB) and Figs. S2a and S2c (measured at HIU) show the plating overpotential as a function of time. Generally, the results obtained from both laboratories are in good agreement. For instance, a larger TEGDME content results in a lower plating overpotential, indicating facilitated plating. Nonetheless, the two compositions with more TEGDME (70:30 and 50:50) exhibit abrupt drops in their potential profiles between 150 and 300 h. These potential drops, highlighted in green in the respective figures, indicate (soft) short-circuiting of the cells.[47] Every five hours, the cells were allowed to rest briefly to equilibrate before conducting EIS. These rest periods explain the periodic potential drops in the voltage profiles. EIS measurements were performed during these rest steps to analyze the impact of the polymer electrolyte composition on the cell impedance and to see how it evolves during lithium plating.

Figures 3d–3f (measured at UCB) and Figs. S2d–S2f (measured at HIU) show the evolution of the Nyquist plots over the duration of the plating experiment. Overall, the total impedance decreases for an increasing TEGDME content, with the resistances being the highest for the 90:10 composition, followed by 70:30, and eventually by 50:50. Comparing the EIS data with the corresponding overpotential profiles reveals a strong correlation. Firstly, irregularities like a distorted high frequency region in the Nyquist plots (compare Fig. 3f inset) coincide with the occurrence of potential drops, which originate from soft-short circuiting (cf Fig. 3c), where the dynamic formation and morphological evolution of localized lithium filaments create fluctuating parallel electronic and ionic pathways and alter the active surface area. Secondly, high resistance values correspond to higher overpotentials, as illustrated in Fig. S3. To gain deeper insights into the underlying processes, distribution of relaxation times analysis (DRT) was performed. In DRT, the impedance spectra are transformed into the time domain using a model composed of parallel resistor–capacitor elements ((R)(C)-elements) in series. Figure 3g shows the DRT plots, obtained after careful adjustment of the regularization parameter λ for the mid-frequency range. In this region, all three materials exhibit a small and a large peak. Based on previous work,[48] the smaller peak (at around 5 10^{-5} s) can be assigned to the charge transfer resistance (R_{CT}), and the larger peak (around 3–5 10^{-4} s) to the SEI resistance (R_{SEI}). In DRT analysis, the peak area corresponds to the magnitude of the resistance, and the peak position indicates the characteristic time constant of the associated physicochemical process. Accordingly, Fig. 3g shows that more TEGDME results in lower resistances and a peak shift to higher frequencies, indicating faster interfacial processes. Generally, the DRT results are in very good agreement with the results of the Nyquist plot fitting that will be discussed in the following (cf Table S2).

To get more quantitative information about the resistances over the 250 h plating period, the EIS data were fitted to a suitable equivalent circuit model, i.e., R-(R)(CPE)-(R)(CPE), as shown in Fig. S4.[48] This model follows our previous work on PEO-based polymer electrolytes, where the use of two (R)(CPE)-elements to describe the intermediate-frequency response is discussed and validated. In this model, CPE denotes a constant phase element, representing non-ideal capacitive behavior. According to Ref.,[48] the resistances are attributed to bulk ionic transport (R_{bulk}), charge transfer (R_{CT}), and transport through the SEI (R_{SEI}). Figure 3h shows the fitted resistance values as a function of time. Consistent with previous observations, this representation illustrates the trend of decreasing resistances for an increasing TEGDME content (R(90:10) > R(70:30) > R(50:50)) for all three resistance types. More liquid plasticizer results in a smaller R_{SEI}, corresponding to facilitated charge transport across the SEI—potentially due to the formation of a less dense and/or more porous SEI with a higher mobility of the lithium-ion coordinating species.[49,50] Additionally, a smaller R_{CT} is observed (inversely proportional to the exchange current density j_0), indicating faster charge transfer kinetics, as well as a smaller R_{bulk}, corresponding to a higher ionic conductivity. R_{bulk} and R_{CT} stay relatively constant during the course of cycling, while R_{SEI} rises during the first

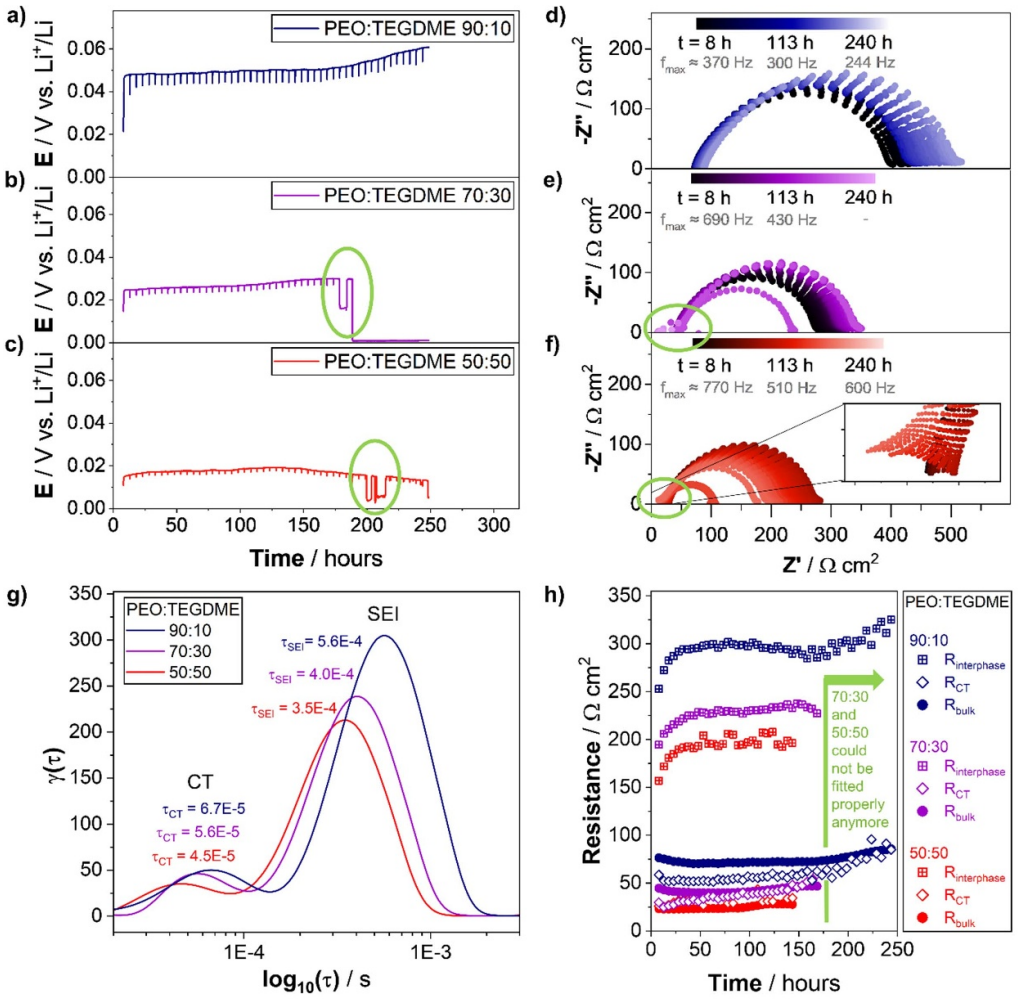

Figure 3. Electrochemical analysis of unidirectional plating in Li||Li cells with the three plasticized polymer electrolytes containing PEO and TEGDME. The experiment was conducted at UCB at 40 °C with a current density of 0.05 mA cm^{-2}. (a)–(c) Plating overpotential profiles over time for the (a) 90:10 (blue), (b) 70:30 (purple), and (c) 50:50 (red) electrolytes. Potential drops due to (soft) short-circuiting are highlighted in green. (d)–(f) Nyquist plots of the EIS data, recorded every five hours during the plating experiment for cells with the (d) 90:10 (blue), (e) 70:30 (purple), (f) and 50:50 (red) composition. Irregularities in the impedance spectra due to (soft) short-circuiting are highlighted in green. (g) DRT analysis for a representative impedance spectrum after 113 h with each electrolyte composition in the mid-frequency range (between 10^{-5} and 10^{-3} s). (h) Resistance values obtained by fitting the impedance spectra during lithium plating with the three different electrolytes (refer to panels (d)–(f)). After approximately 175 h, (soft) short-circuiting of the cells with the 70:30 and 50:50 electrolytes prevented meaningful fitting, as indicated in green.

hours, before transitioning into a plateau after approximately 50 h. To validate these trends, the same experiment was also conducted at HIU (see Figs. S5a–S5c), and under storage conditions (see Figs. S5d–S5f). As evident from Fig. S5, the above-mentioned resistance trends obtained during plating at UCB (compare Fig. 3h) could be reproduced at HIU and were also confirmed during storage, which ruled out large distortions from lithium plating. These consistent results across different conditions and laboratories confirm the reliability of the observed resistance trends during the plating experiment that, as we suspect, originate in the greater mobility of TEGDME (fragments) in the bulk of the electrolyte and in the interface/-phase region. Nevertheless, the resistance values provide only averaged information across the whole active cell area. Therefore, it is not fully certain if or to what extent local inhomogeneities, such as thinner SEI regions or TEGDME-rich (pore-type) transport pathways that would reduce the respective resistances, may influence the impedance response and the long-term stability of the lithium-metal anode.

While it is tempting to postulate changes in the nature of the plating electrode based entirely on current–voltage relationships, we chose to study the nature, morphology and spatial distribution of the plated lithium after the unidirectional plating experiments directly using the nondestructive X-ray tomography imaging technique. This approach enables the direct visualization of the actual deposition structures formed at the end of the 250 h plating period.

Figure 4 shows the cross-sectional tomography images obtained for the three types of electrolytes (90:10, 70:30, and 50:50). In these diagrams, lithium is stripped from the top electrode and plated on the bottom electrode. Typical tomograms are shown in panels a, c, and g. The stripping electrode is smooth in all cases, with occasional globules as shown in panels b, d, and h. The main observation, however, is that the roughness of the plating electrode increases with increasing TEGDME content (compare panels a, c, and g). In addition, cells with the 70:30 and 50:50 electrolytes also show multiglobular and mossy structures growing into the electrolyte. In the 50:50 electrolyte material, some of these features spanned the

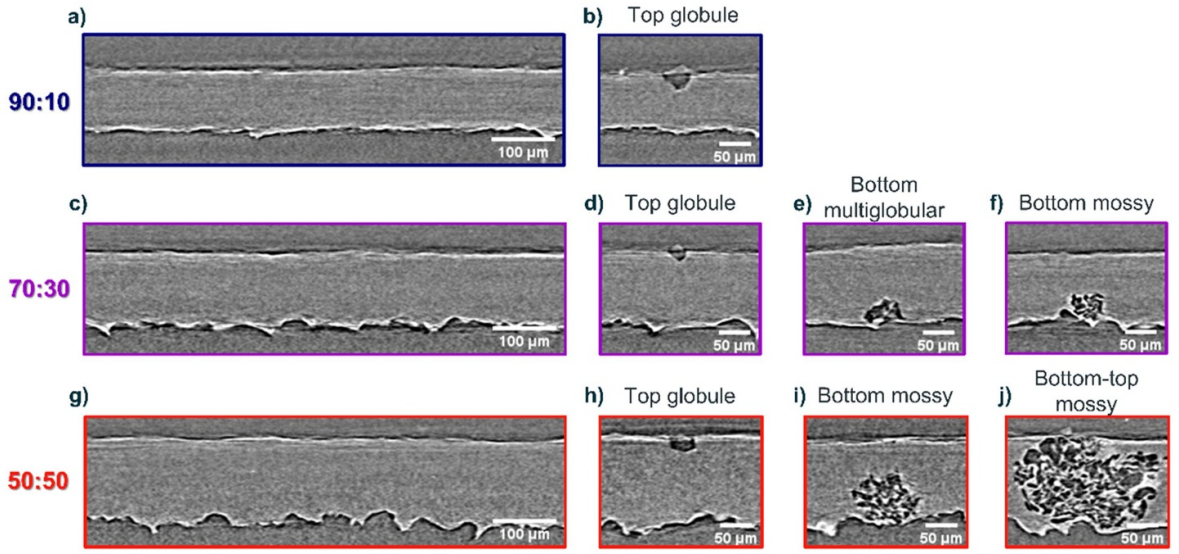

Figure 4. Cross-sectional tomography images after plating a capacity of 12.5 mAh at 40 °C in Li||Li cells using the three different PEO:TEGDME electrolytes with weight ratios of (a) and (b) 90:10 (blue), (c)–(f) 70:30 (purple), and (g)–(j) 50:50 (red). Lithium was plated from top to bottom. The left panels show a representative section for each cell, illustrating the respective plating morphologies at the bottom. The right panels show additional typical features found in the tomography images, including (b)–(h) globules at the top electrode, (e) multiglobular structures at the bottom electrode, (f) and (i) mossy lithium formation at the bottom electrode, and (j) large mossy structures reaching from the bottom to the top electrode.

whole electrolyte. Since these large mossy structures likely connect both lithium-metal electrodes electrically, it explains the sudden potential drops and the irregularities in the EIS data due to cell shorting.

Figure 5 quantifies the relative density of the features at the bottom interface labeled as "bottom multiglobular", "bottom mossy", and "bottom-top mossy" depending on their location and type. It shows that the fraction and size of globular and mossy features increases with higher TEGDME content in the electrolyte. While it is qualitatively apparent that the 50:50 electrolyte shows more inhomogeneous plating and a rougher interface at the plating electrode, it is also important to quantify the surface roughness based on the tomographic images. To do this, the tomographic images were segmented to define the local thickness of the electrolyte using the Weka 3D Segmentation Plugin for ImageJ. The average thickness L_{avg} of our 50:50, 70:30, and 90:10 samples was 133, 133, and 93 μm. These values were subtracted from each of our point-wise thickness of the electrolyte L_i to compute a parameter that we call relative interfacial growth (*RIG*), for which we refer to the ordinate in Fig. 6b for the sake of simplicity. Areas that contained multiglobular and mossy structures were excluded from *RIG* calculations. Our objective was to quantify the general roughness differences in the three cases (Figs. 4a–4g). If plating were perfectly uniform, all *RIG* values would be zero. The larger the magnitude of *RIG*, the larger the local plating nonuniformity. Quantitatively *RIG* is defined at each voxel along the x–y plane, i, as:

$$RIG_i = L_{avg} - L_i \qquad [15]$$

Positive values of RIG_i represent peaks, while negative values signify valleys (cf Fig. 6a). When we analyze the plating at a given surface, we obtain a range of RIG_i values. Figure 6b shows the distributions of RIG_i values obtained for the three electrolytes. We report on RIG_i values that fall within the 5th–95th percentile. For concreteness, let us consider the 50:50 dataset. At quantile = 0.2, the reported value is -10 μm. This implies that 20% of the RIG_i values for this electrolyte have valleys that are deeper than 10 μm. At quantile = 0.8, the reported value is $+12$ μm. This implies that

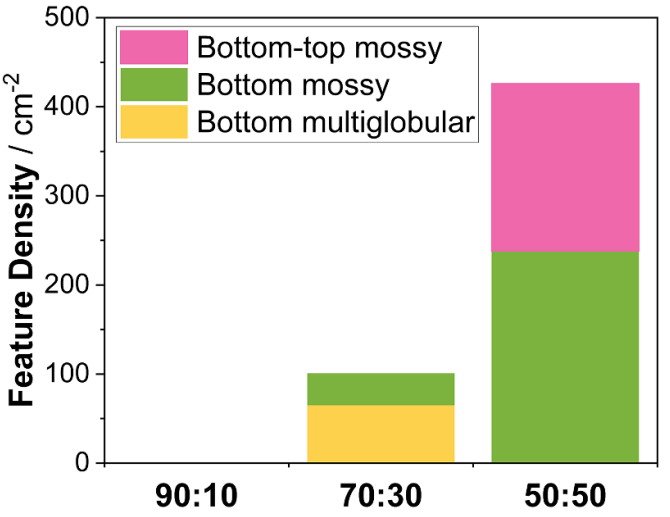

Figure 5. Quantification of the density of the features observed at the bottom electrode in the tomography images after plating in Li ||Li cells using the three PEO:TEGDME electrolytes with different weight ratios (90:10, 70:30, and 50:50). The features quantified in this bar chart are mutliglobular (yellow) and mossy (green) structures, potentially spanning from the bottom to the top electrode (pink).

80% of the RIG_i values for this electrolyte have either peaks with heights less than 12 μm or valleys. In other words, 20% of the area of the electrode for the 50:50 electrolyte has peaks higher than 12 μm. In comparison, for the 90:10 electrolyte, at quantile = 0.8, the reported value is $+6$ μm. In this case, 20% of the area of the electrode has peaks higher than 6 μm. Based on Fig. 6b, we can quantitatively conclude that the roughness of the electrode increases with TEGDME content. This conclusion holds regardless of the chosen quantile.

In order to visualize the dependence of the electrode roughness on the TEGDME content, we computed the standard deviation of the

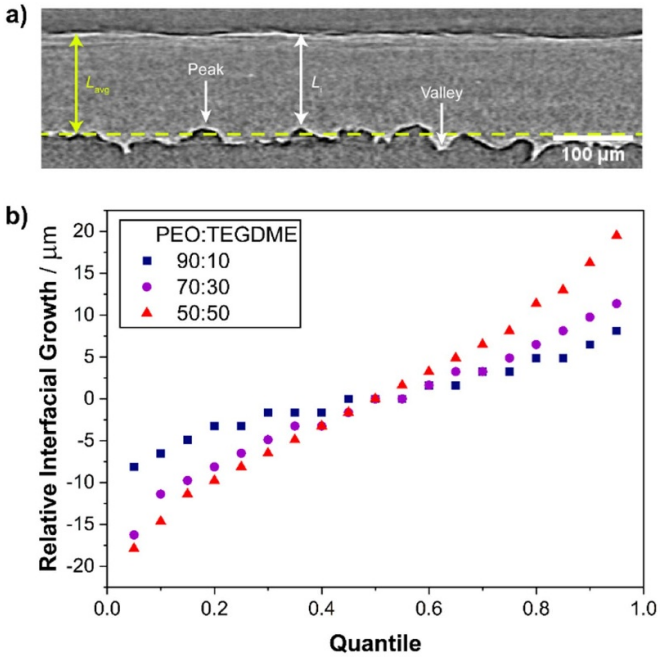

Figure 6. Relative interfacial growth (*RIG*) determination of plated lithium in Li||Li cells. (a) Schematic of our definition of "peaks" and "valleys" as well as L_{avg} and L_i used to calculate the *RIG*. (b) Results of the *RIG* for each quantile across all three electrolyte compositions with PEO:TEGDME ratios of 90:10 (blue), 70:30 (purple), and 50:50 (red). Data are limited to the 5th–95th percentile to exclude outliers.

electrolyte thickness, ν. If we were to plot pixel-based deviations, the images would be dominated by outliers. We can instead use averages over squares with fixed dimensions to define a local and global standard deviation. ν is thus defined as:

$$\nu = \left(\frac{\sum_1^n \left(L_{\text{avg}} - L_i\right)^2}{n-1} \right)^{1/2} \quad [16]$$

where $n = 41$ μm (25 pixels) is used to compute the local standard deviation, and $n = 730$ μm (450 pixels) to compute the global standard deviation. The global standard deviation is equivalent to taking the standard deviation based on the average electrolyte thickness over the entire electrode area, while the local standard deviation iteratively calculates the standard deviation based on the local average electrolyte thickness.

In Fig. 7, we show heat maps of the local standard deviation as a function of x and y with 3D renderings of small but representative portions of the electrode shown alongside the heat maps. Areas that contained multiglobular and mossy structures were excluded from the deviation calculations. The averages of the local standard deviations are 2.4 μm for 90:10, 3.0 μm for 70:30, and 6.2 μm for 50:50. It is clear from Fig. 7 that the 50:50 electrolyte gives the roughest lithium electrode. The roughness of the 70:30 and 90:10 electrodes look similar when examined by these heat maps. The global standard deviations of electrolyte thickness for the entire electrode area shown in Fig. 7 are 5.1 μm for 90:10, 8.2 μm for 70:30 and 12 μm for 50:50 samples.

In sum, the experiments show a systematic increase in surface roughness with an increasing plasticizer content regardless of the measure, i.e., whether *RIG* or ν.

Modeling.—To further analyze and understand the morphologies observed in the tomography images, lithium plating was modeled with the three different electrolytes. For this, the growth of an initial

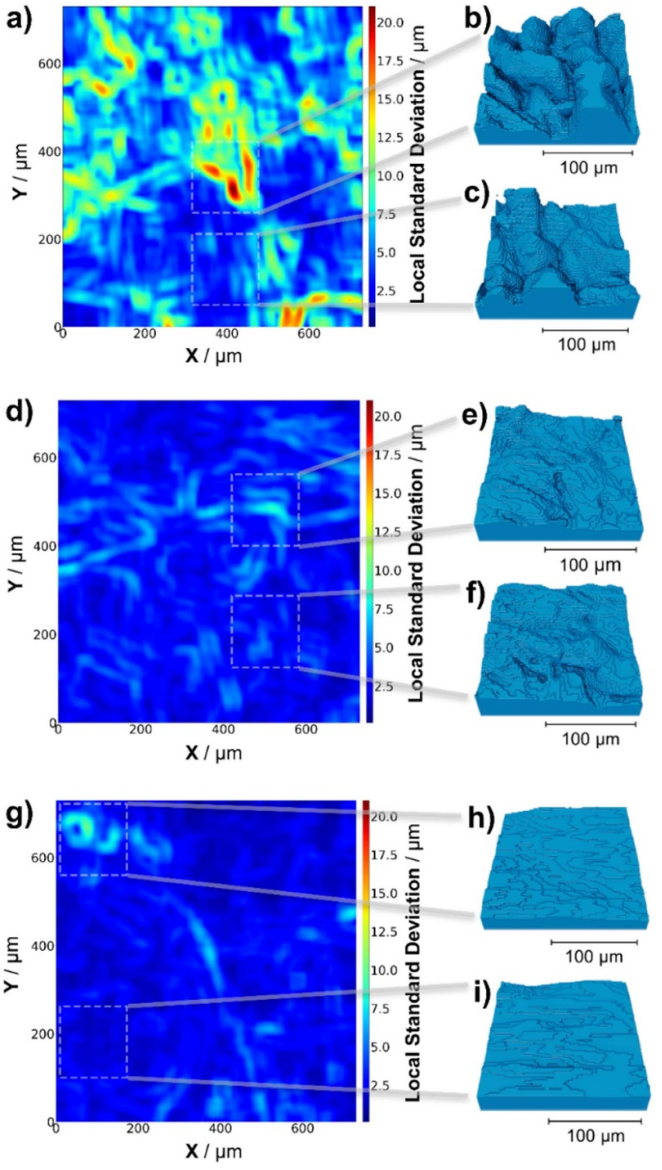

Figure 7. Plating morphology analysis based on the tomography images after plating 12.5 mAh at 40 °C in Li||Li cells with the electrolyte compositions (a)–(c) 50:50, (d)–(f) 70:30, and (g)–(i) 90:10 (see Fig. 4. Panels on the left: Mappings of the local standard deviation of the electrolyte thickness (based on the average electrolyte thickness over areas of 25 by 25 pixels) as a function of x and y. Panels on the right: 3D renderings of a rough (top) and smooth (bottom) region of the electrode.

lithium metal protrusion (see Fig. S6a) was investigated during constant current application, taking into account the different mechanical properties of these electrolytes in the model. As evident from Fig. 8 and Figs. S6b and S6c, during the 250 h of plating, the protrusion grows higher for an increasing TEGDME content. With an increasing plasticizer content, the polymer electrolytes become more compliant, which accelerates protrusion growth. In contrast, the 90:10 material, with the highest Young's modulus, shows the slowest increase in protrusion height. The model thus captures the mechanical stress-induced suppression of the protrusion growth. Interestingly, other electrolyte-related parameters, such as their exchange current density (Table S5), electrolyte thickness, or ionic conductivity exert only negligible influence on the protrusion evolution during the plating period (see Fig. S7), while a potentially less dense SEI in the case of higher TEGDME contents might also have an effect.

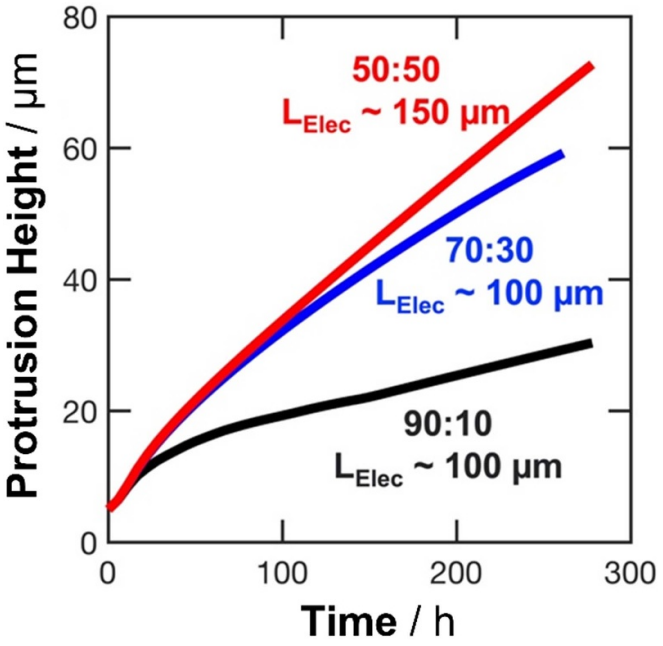

Figure 8. Modeling results showing the evolution of a lithium-metal protrusion height (see Fig. S6) under unidirectional current in the three electrolytes with different mechanical properties and thicknesses. The height of the dendritic protrusions is plotted as a function of time with the different PEO:TEGDME electrolytes in weight ratios of 90:10 (blue), 70:30 (purple), and 50:50 (red).

Table I. Summary of material properties and plating characteristics for the studied PEO:TEGDME electrolytes.

Sample	$i_L d$ / mA cm^{-1}	E / MPa	Time till cell failure / h	Theoretical protrusion height at failure time /μm	*RIG* difference between 5th and 95th quantile /μm	Bottom mossy feature density / cm^{-2}
50:50	0.020	0.13	200	58	37	250
70:30	0.010	0.31	175	45	28	30
90:10	0.005	0.62	>250	30	16	0

Although the model assumes uniform deposition outside the initial protrusion (see Eq. 9), and does not explicitly model variations in electrolyte thickness or electrode surface roughness, the simulation results are in good agreement with the experimental observations. Table I summarizes the key parameters from both modeling and experiments. Notably, the *RIG*-based surface roughness values (16–37 μm) fall within a similar range as the predicted protrusion heights after about 200 h (30–58 μm), with both increasing monotonically with the TEGDME content. This consistency highlights the strong parallels between the model predictions and the tomography results. Extending from the modeling observations, we conclude that the differences in plating morphology observed in the tomography images primarily originate from the varying mechanical properties of the three electrolytes.

Conclusions

In this study, we investigated the impact of the TEGDME plasticizer content in crosslinked PEO-based electrolytes on the lithium plating behavior via a combined experimental and theoretical approach. The comprehensive electrochemical characterization of the charge transport within the bulk electrolyte and at the electrode|electrolyte interface reveals that a higher TEGDME content results in an increased ionic conductivity, diffusion coefficient, and limiting current density, and a decreased interfacial resistance, while the Li^+ transference number remained essentially unaffected. In contrast, though, the mechanical stiffness and strength of the plasticized polymer electrolytes decreased with an increasing TEGDME content. In other words, the improvement of electrochemical properties due to the addition of a plasticizer comes at a disproportionate cost of deterioration of mechanical properties. While these results are somehow expected, the surprising finding, obtained via ex situ X-ray tomography, is that the morphology of the plated lithium becomes increasingly globular and mossy, i.e., rougher and more uneven, for an increasing TEGDME content—despite the superior charge transport properties in the bulk and at the interface. In fact, theoretical calculations confirm that the key factor for achieving smooth lithium deposition in such electrolyte systems is the mechanical stiffness rather than the given electrochemical properties. We may anticipate that this finding, highlighting the importance of mechanical electrolyte properties, will be of great help for designing advanced lithium battery polymer electrolytes.

Acknowledgments

This work was funded by the US-German collaboration on "Interfaces and Interphases in Rechargeable Li-metal based Batteries" in the frame of the joint research project "LISI(−2)" by the German Federal Ministry of Education and Research (BMBF), now the German Federal Ministry of Research, Technology and Space (BMFTR; 03XP0224D and 03XP0509D) and the U.S. Department of Energy under the Advanced Battery Materials Research Program (BMR; DOE; DE-AC02-05CH11231 and DE-AC02-06CH11357). K.G. would also like to thank the Studienstiftung des deutschen Volkes for its financial support.

Authorship contribution statement

The study was initiated by N.B. and D.B. and designed jointly by D.S., V.P., and K.G., with input and supervision from N.B. and D.B. The electrochemical and mechanical characterization was performed by K.G., V.P., D.S., and M.J. Tomography was conducted by V.P. and data analysis was carried out by K.G., V.P., D.S., and M.B. P.B. conducted the modeling under the supervision of V.S. Following joint discussions about the results, K.G. prepared the first draft of the manuscript with contributions from V.P., D.S., and P.B. All authors reviewed, edited, and approved the final version of the manuscript.

ORCID

Katrin Geng https://orcid.org/0000-0003-4347-4225
Vivaan Patel https://orcid.org/0000-0002-7591-7353
Dominik Steinle https://orcid.org/0000-0001-8137-9646
Pallab Barai https://orcid.org/0000-0003-2217-6392
Medina Jasarevic https://orcid.org/0009-0007-5113-4956
Michael Bowen https://orcid.org/0000-0001-5380-7383
Venkat Srinivasan https://orcid.org/0000-0002-1248-5952
Nitash Balsara https://orcid.org/0000-0002-0106-5565
Dominic Bresser https://orcid.org/0000-0001-6429-6048

References

1. J. Xie and Y.-C. Lu, *Nat. Commun.*, **11**, 2499 (2020).
2. J. Betz, G. Bieker, P. Meister, T. Placke, M. Winter and R. Schmuch, *Adv. Energy Mater.*, **9**, 1803170 (2019).
3. S. Choudhury, S. Stalin, D. Vu, A. Warren, Y. Deng, P. Biswal and L. A. Archer, *Nat. Commun.*, **10**, 4398 (2019).
4. J. Janek and W. G. Zeier, *Nat. Energy*, **1**, 16141 (2016).
5. X. Cui, J. Wang, S. Sun, X. Chen, Y. Wang, D. Han, J. Wang, X. Yao and W. Yan, *Energy Fuels*, **39**, 7665 (2025).
6. P. Lennartz, B. A. Paren, A. Herzog-Arbeitman, X. C. Chen, J. A. Johnson, M. Winter, Y. Shao-horn and G. Brunklaus, *Joule*, **7**, 1471 (2023).
7. G. Yang, M. L. Lehmann, S. Zhao, B. Li, S. Ge, P.-F. Cao, F. M. Delnick, A. P. Sokolov, T. Saito and J. Nanda, *Energy Storage Mater.*, **35**, 431 (2021).
8. M. Marzantowicz, J. R. Dygas, F. Krok, J. L. Nowiński, A. Tomaszewska, Z. Florjańczyk and E. Zygadło-Monikowska, *J. Power Sources*, **159**, 420 (2006).
9. M. S. Ding, K. Xu, S. S. Zhang, K. Amine, G. L. Henriksen and T. R. Jow, *J. Electrochem. Soc.*, **148**, A1196 (2001).
10. J.-M. Tarascon, A. S. Gozdz, C. Schmutz, F. Shokoohi and P. C. Warren, *Solid State Ion.*, **86–88**, 49 (1996).
11. J. Castillo et al., *Chem. Mater.*, **33**, 8812 (2021).
12. L. Carbone, M. Gobet, J. Peng, M. Devany, B. Scrosati, S. Greenbaum and J. Hassoun, *ACS Appl. Mater. Interfaces*, **7**, 13859 (2015).
13. M. L. Lehmann et al., *Energy Storage Mater.*, **21**, 85 (2019).
14. Z. Du et al., *J. Electrochem. Soc.*, **168**, 050549 (2021).
15. Z. Chen, J. Li, F. Qiu, C. Lu, J. Zhu and X. Zhuang, *J. Mater. Chem. A*, **10**, 14849 (2022).
16. L. Chen et al., *Nat. Commun.*, **16**, 3517 (2025).
17. R. Khurana, J. L. Schaefer, L. A. Archer and G. W. Coates, *J. Am. Chem. Soc.*, **136**, 7395 (2014).
18. C. Monroe and J. Newman, *J. Electrochem. Soc.*, **152**, A396 (2005).
19. Y. Wang, J. Wu, W. Chen, Z. Jiang and Z. Jiang, *Small*, **22**, e13300 (2026).
20. B. Zhang, B. Yuan, X. Yan, X. Han, J. Zhang, H. Tan, C. Wang, P. Yan, H. Gao and Y. Liu, *Nat. Commun.*, **16**, 1906 (2025).
21. P. Röring, J. Pleie, A. J. Butzelaar, G. M. Overhoff, C. Schmidt, K. Neuhaus, P. Théato, M. Winter and G. Brunklaus, *J. Am. Chem. Soc.*, **148**, 4176 (2026).
22. B. Li et al., *Electrochem. Energy Rev.*, **6**, 7 (2023).
23. B. Horstmann et al., *Energy Environ. Sci.*, **14**, 5289 (2021).
24. G. T. Kim, G. B. Appetecchi, M. Carewska, M. Joost, A. Balducci, M. Winter and S. Passerini, *J. Power Sources*, **195**, 6130 (2010).
25. K. Geng et al., *J. Electrochem. Soc.*, **169**, 110521 (2022).
26. P. G. Bruce, M. T. Hardgrave and C. A. Vincent, *Solid State Ion.*, **53–56**, 1087 (1992).
27. P. G. Bruce and C. A. Vincent, *J. Electroanal. Chem.*, **225**, 1 (1987).
28. P. Bruce, *Solid State Ion.*, **28–30**, 918 (1988).
29. S. D. Thompson and J. Newman, *J. Electrochem. Soc.*, **136**, 3362 (1989).
30. M. Braig and R. Zeis, *J. Power Sources*, **576**, 233203 (2023).
31. P. Barai, K. Higa, A. T. Ngo, L. A. Curtiss and V. Srinivasan, *J. Electrochem. Soc.*, **166**, A1752–A62 (2019).
32. C. Monroe and J. Newman, *J. Electrochem. Soc.*, **151**, A880 (2004).
33. A. Mistry and P. P. Mukherjee, *J. Electrochem. Soc.*, **167**, 082510 (2020).
34. V. St-Onge, M. Cui, S. Rochon, J.-C. Daigle and J. P. Claverie, *Commun. Mater.*, **2**, 83 (2021).
35. Y. Guo, X. Qu, Z. Hu, J. Zhu, W. Niu and X. Liu, *J. Mater. Chem. A*, **9**, 13597 (2021).
36. H. Wang, M. Matsui, Y. Takeda, O. Yamamoto, D. Im, D. Lee and N. Imanishi, *Membranes*, **3**, 298 (2013).
37. L. Porcarelli, C. Gerbaldi, F. Bella and J. R. Nair, *Sci. Rep.*, **6**, 19892 (2016).
38. M. M. Hiller, M. Joost, H. J. Gores, S. Passerini and H.-D. Wiemhöfer, *Electrochim. Acta*, **114**, 21 (2013).
39. L. Bertoli, G. Gabriele, E. Gibertini and L. Magagnin, *J. Energy Storage*, **81**, 110456 (2024).
40. B. B. Jing and C. M. Evans, *J. Am. Chem. Soc.*, **141**, 18932 (2019).
41. M. Patel and A. J. Bhattacharyya, *Electrochem. Commun.*, **10**, 1912 (2008).
42. A. R. Polu and H.-W. Rhee, *J. Ind. Eng. Chem.*, **31**, 323 (2015).
43. J.-N. Chazalviel, *Phys. Rev. A*, **42**, 7355 (1990).
44. A. J. Bard, G. Inzelt and F. Scholz, Eds., *Electrochemical Dictionary*, 2nd ed., p. 1, Springer, Berlin Heidelberg (2012).
45. P. Barai, K. Higa and V. Srinivasan, *Phys. Chem. Chem. Phys.*, **19**, 20493–505 (2017).
46. V. Patel et al., *J. Electrochem. Soc.*, **168**, 120546 (2021).
47. S. Menkin, J. B. Fritzke, R. Larner, C. De Leeuw, Y. Choi, A. B. Gunnarsdóttir and C. P. Grey, *Faraday Discuss*, **248**, 277 (2024).
48. K. Geng, B. A. Tappan, S. Passerini, Y. Shao-horn and D. Bresser, *Adv. Sci.*, **13**, e14492 (2025).
49. J. Grill and J. Popovic-Neuber, *Commun. Chem.*, **7**, 297 (2024).
50. K. Lim, B. Fenk, J. Popovic and J. Maier, *ACS Appl. Mater. Interfaces*, **13**, 51767 (2021).